Convective Self-Aggregation Occurs Without Radiative Feedbacks in Warm Climates

Lin Yao*[1] and Da Yang*[1,2]

[1]University of California, Davis, CA, USA.

[2]Lawrance Berkeley National Laboratory, Berkeley, CA, USA.

* *Corresponding authors:* Lin Yao, linyao@ucdavis.edu, Da Yang, dayang@ucdavis.edu

Key Points:

- Radiative feedbacks become less important to the development of convective self-aggregation (CSA) with surface warming.
- In warm climates, CSA can still occur without radiative feedbacks.
- Radiative feedbacks influence the horizontal scale of CSA, although they are not essential to CSA development in warm climates.

Abstract

Previous research showed that radiative feedbacks are essential to the spontaneous development of convective aggregation (CSA) in idealized atmosphere models. We find that the contribution of radiative feedbacks decreases with warming and that, in warm climates, CSA occurs without radiative feedbacks. We perform 2D simulations in different climates using a cloud-resolving model and use a local moist static energy (LMSE) framework to quantify the contribution of radiative feedbacks to the increase of LMSE variance, which characterizes the development of CSA. The result shows that radiative contribution dominates the LMSE variance production when SST is less than 300 K; when SST is higher than 300 K, adiabatic variance production becomes more important than radiative production. Then we turn off radiative feedbacks by horizontally homogenizing radiative heating rates at all model levels. CSA still occurs in warmer climates (310–320 K). This result agrees with the LMSE diagnosis and additional 3D simulations.

Plain Language Summary

Convective clouds often come together and combine to create larger storms. Previous research indicated that this aggregation is mainly driven by a feedback loop influenced by atmospheric radiation. However, our study reveals that this feedback mechanism becomes less effective as the climate warms. In particular, in a warmer climate where surface temperatures are around 10 or 20 degrees higher than present, convective clouds can still aggregate even in the absence of this radiative feedback loop. These findings are derived from atmosphere simulations at high resolution and analyses of the variability of moist static energy at different altitudes.

1. Introduction

In cloud-resolving simulations, the atmosphere tends to spontaneously organize into distinct moist and dry regions over a uniform sea surface temperature (SST). This moisture organization is associated with the development of persistent large-scale circulations and is known as convective self-aggregation (CSA). In the moist regions, deep convective storms are ubiquitous; in the dry regions, subsidence prevails. Previous research has shown that both tropical cyclones (TCs) and the Madden-Julian Oscillation (MJO) can be simulated with uniform boundary conditions (e.g., uniform SST) over f-plane and beta-plane, respectively (Bretherton et al., 2005; Nolan et al., 2007; Boos et al., 2016; Arnold and Randall, 2015). These results suggested that TCs and the MJO may be organized by similar processes on a much larger scale. Therefore, understanding CSA better may help enhance our knowledge of TCs and the MJO.

Previous research has repeatedly shown that radiative feedbacks are essential to the development of CSA using numerical experiments (e.g., Bretherton et al., 2005; Muller and Held, 2012) and the moist static energy (MSE) variance analysis (Andersen and Kuang, 2012; Wing and Emanuel, 2014; Coppin and Bony, 2015; Arnold and Randall, 2015; Wing and Cronin, 2016; Pritchard and Yang, 2016; Holloway and Woolnough, 2016). Although which radiative process dominates CSA is still under debate, all these studies agreed that radiative feedbacks made important contributions to the MSE variance budget and that CSA cannot occur if radiative feedbacks are fully disabled. Meanwhile, the dependence of the role of radiative feedbacks on SSTs was investigated using general circulation models (GCMs) and cloud-resolving models (CRMs) (Coppin and Bony, 2015; Wing and Cronin, 2016; Pope et al., 2021; Pope et al., 2023). The results also showed that radiative

feedbacks are important to trigger and maintain CSA over a wide range of climates (e.g., 280-310 K), although their role was noted to decrease with SSTs.

Despite the high degree of consensus using CRM and GCM simulations, a variety of simple models suggest that CSA may occur without radiative feedbacks (Muller et al., 2022). For example, Craig and Mack (2013) and Windmiller and Craig (2019) used a reaction-diffusion equation to simulate the upscale growth in CSA. They showed that CSA could be driven by a positive moisture-entrainment feedback (Tompkins, 2001; Yang, 2019). Moreover, Haerter (2019) proposed that convection-induced cold pools can mechanically lift boundary layer air parcels and trigger convection in nearby regions, forming CSA. Additionally, Yang (2021) found that CSA could occur in a 1D shallow-water model with triggered convection. In his model, there is no radiative feedback, and the persistent moist convecting regions and dry subsiding regions can result from interference of convectively coupled gravity waves. All these simple models imply that radiative feedbacks may not be essential for the development of self-aggregation in theory, while there have not been CRM or GCM studies supporting this conclusion.

This paper reports that CSA can still emerge without radiative feedbacks in CRM simulations with high SSTs. To demonstrate this, we conduct a series of mechanism-denial experiments in CRM simulations over a wide range of climates using both 2D and 3D domains. We will also apply a vertically resolved MSE variance analysis (Yao, Yang, and Tan, 2022)—in contrast to the conventional MSE variance analysis in Wing and Emanuel (2014)—to examine the role of radiative feedbacks on the development of CSA in individual climate states. Section 2 will introduce the vertically resolved MSE variance framework in detail. Section 3 will introduce the

model setup and metrics to quantify CSA. Section 4 will show the main results. We summarize our findings and discuss their implications in Section 5.

2. The vertically resolved MSE variance framework

Previous research widely used a vertically integrated MSE variance framework to study CSA (Andersen and Kuang, 2012; Wing and Emanuel, 2014; Coppin and Bony, 2015; Holloway and Woolnough, 2016; Pope et al., 2023). They measured the development of CSA as an increase of the vertically integrated MSE variance and assessed diabatic and adiabatic (advective) contributions to the variance increase. In this approach, the vertical integral of MSE was first performed, and then its horizontal variance was calculated. As a result, such calculated MSE variance consists of both the local MSE (LMSE) variance at a given altitude and the covariance between different vertical levels (Equation (10) in Yao, Yang and Tan, 2022). Thus, this MSE variance is referred to as the global MSE variance. This method implicitly assumes that the vertical structures of MSE anomaly and its sources are not fundamental to CSA. However, Mapes (2016) argued that the vertical dimension is too important to be integrated over, and growing evidence has shown that boundary layer processes are particularly important to CSA development (Muller and Held, 2012; Mapes, 2016; Yang, 2018b; Yao, Yang and Tan, 2022).

Here we apply the recently developed LMSE variance framework to study CSA (Yao, Yang and Tan, 2022). In the LMSE framework, we first calculate horizontal MSE variance for individual vertical layers, and then we perform the vertical integral. Although this procedure seems only slightly different from that of the global MSE analysis, the two approaches are conceptually different. For example, the LMSE analysis respects the characteristic vertical structure of CSA and

does not concern covariance terms across different altitudes. A detailed discussion of the LMSE analysis and its comparison to the conventional global MSE analysis can be found in Yao, Yang and Tan (2022). The framework has also been applied to study TCs and the MJO recently (Zhang et al., 2022; Yang and Hannah, 2022).

Since CSA is a long-lasting, large-scale phenomenon, we apply both temporal and spatial running averages to variables to filter out small-scale and high-frequency signals. We test the robustness of our results using the temporal window width varying from 1, 3, 5, to 10 days, and the spatial window width varying from 40, 88, to 120 km. The uncertainty of the results is shown as error bars in Figure 2.

We introduce the LMSE framework in an anelastic atmosphere. We integrate the LMSE variance at individual layers from the surface to the tropopause, which is defined using temperature minimum. The LMSE variance in the troposphere is given by

$$\mathrm{var}(h') = \frac{1}{2}\int_0^{z_t} \rho_0 \overline{(h')^2}\, dz, \tag{1}$$

where h' is the large-scale MSE anomalies at individual layers, z_t is the height of the tropopause, and $\rho_0 = \rho_0(z)$ is the reference density at individual layers in an anelastic atmosphere. Note Equation (1) is weighted by ρ_0 instead of ρ_0^2 as in Yao, Yang and Tan (2022). Then if we divide Equation (1) by the total column mass, we get a quantity with a unit of energy variance, consistent with Yang and Hannah (2022). The budget equation for the LMSE variance in the troposphere is given by

$$\underbrace{\partial_t\big(\mathrm{var}(h')\big)}_{\substack{\text{variance}\\ \text{tendency}}} = \underbrace{\int_0^{z_t} \rho_0 \overline{h'[-u\partial_x h - w\partial_z h]'}dz}_{\substack{\text{adiabatic production}\\ \text{(horizontal+vertical)}}} + \underbrace{\int_0^{z_t} \rho_0 \overline{h'Q'_{rad}}dz}_{\substack{\text{radiative}\\ \text{production}}} + \underbrace{\int_0^{z_t} \rho_0 \overline{h'Q'_{sgs}}dz}_{\substack{\text{SGS}\\ \text{production}}}. \quad (2)$$

Here, (u, w) are the wind speeds. The adiabatic production includes variance production from both horizontal and vertical advection anomalies of LMSE. $\left(Q'_{rad},\ Q'_{sgs}\right)$ are the anomalies of LMSE sources due to radiation and sub-grid scale (SGS) processes (Units: W m^{-2}). These anomalies of LMSE advection and sources are co-located with the LMSE anomalies to generate or consume LMSE variance. For example, additional radiative cooling ($Q'_{rad} < 0$) in dry regions ($h' < 0$) leads to an increase in the LMSE variance, promoting the development of CSA.

If we assume the horizontal SGS MSE flux convergence is negligible, then the SGS MSE tendency is dominated by the vertical SGS MSE flux convergence, which is $Q_{sgs} = -\frac{1}{\rho_0}\partial_z F$ (F is MSE flux; Yao, Yang and Tan, 2022), then the total SGS production of LMSE variance can be further decomposed into two parts:

$$\begin{aligned}\int_0^{z_t} \rho_0 \overline{h'Q'_{sgs}}dz &= \int_0^{z_t} \overline{h'(-\partial_z F')}dz = -\int_0^{z_t} \overline{\partial_z(h'F')}dz + \int_0^{z_t} \overline{F'\partial_z(h')}dz \\ &= \overline{h'F'|_{z=0}} + \int_0^{z_t} \overline{F'\partial_z(h')}dz. \end{aligned} \quad (3)$$

142 The first term on the right-hand side appears to be the variance production from surface fluxes. It
143 can be numerically calculated as the product of the MSE anomaly at the lowest model level and
144 the anomaly of surface fluxes. The second term is the variance production from the remaining SGS
145 processes. In a mixed-layer limit ($\partial_z(h') = 0$), the second term vanishes. It becomes clear that the
146 first term represents both local impact from surface fluxes and non-local impact due to mixing.
147
148 This study investigates the development of CSA over a wide range of climates, whose LMSE
149 variances in equilibrium are different. To compare among different climates, we normalize
150 Equation (2) with the LMSE variance in the troposphere at each time step. The normalized budget
151 is given by
152

$$\frac{\partial_t\big(\mathrm{var}(h')\big)}{\mathrm{var}(h')} = \frac{\int_0^{z_t} \rho_0 \overline{h'[-u\partial_x h - w\partial_z h]'}dz}{\mathrm{var}(h')} + \frac{\int_0^{z_t} \rho_0 \overline{h'Q'_{rad}}dz}{\mathrm{var}(h')} + \frac{\int_0^{z_t} \rho_0 \overline{h'Q'_{sgs}}dz}{\mathrm{var}(h')}. \qquad (4)$$

153
154 The left-hand side of Equation (4) represents the growth rate of CSA, which is measured by the
155 fractional change of the LMSE variance in the whole troposphere per unit time. The terms on the
156 right-hand side represent individual contributions to the growth rate from the adiabatic production,
157 radiative production, and SGS production. Note the adiabatic production is from both horizontal
158 and vertical advection anomalies of LMSE. In our following analysis, we will explicitly calculate
159 the horizontal advection of LMSE and calculate the vertical advection as a residual of the LMSE
160 budget equation, since the LMSE budget is exactly conserved in our model (Khairoutdinov and
161 Randall, 2003). We choose this calculation method due to the challenge of closing the LMSE
162 budget using infrequent output to calculate the advection of MSE (Bretherton et al., 2005).
163

3. Model and Method

3.1 Model setup

We use the System for the Atmospheric Modeling (SAM; version 6.10.10) to perform 2D and 3D simulations in this paper. SAM is an anelastic cloud-resolving model (Khairoutdinov and Randall, 2003). It solves the conservation law for momentum, mass, the frozen MSE, total non-precipitating water (water vapor, cloud water, and cloud ice), and total precipitating water (rain, snow, and graupel).

Here we first perform 2D simulations using a periodic domain in x. The domain size is 16,384 km, with a horizontal resolution of 2 km. The model top is at 33 km, with 128 vertical levels. Below 16 km, the vertical grid is identical to that in cloud-resolving experiments in the Radiative-Convective Equilibrium Model Intercomparison Project (RCEMIP, Table 3 in Wing et al., 2020). The vertical resolution increases from 40 m near the surface to 200 m above 3 km. Above 16 km, the vertical resolution gradually increases to 500 m. Newtonian damping is applied to the top 10 km to reduce the reflection of gravity waves. The radiative transfer scheme is the same as that of the Community Atmosphere Model (CAM3; Collins et al., 2006). The solar insolation is set to 424.5 W m^{-2} to represent the climatological value in the tropics. We turn off the diurnal cycle for simplicity. The microphysics is the one-moment parameterization. In the microphysical scheme, the non-precipitating water (clouds) and precipitating water (precipitation) can be further partitioned into liquid and ice phases based on temperature. The SGS processes use SAM Smagorinsky parameterization to represent turbulent fluxes in the atmosphere and use the Monin-Obukhov similarity theory and bulk formula to calculate turbulent surface fluxes. We show simulations with five different sea surface temperatures (SSTs) in the main text: 280 K, 290 K,

300 K, 310 K, 320 K. We also include simulations at 315 K in the Supporting Information to show the robustness of our findings. Each simulation runs for 150 days over a uniform SST. To examine the role of radiative feedbacks, we also perform mechanism-denial experiments at each SST. In these simulations, we horizontally homogenize radiative heating rates at all model levels each time the model updates radiative heating profiles.

We also perform a pair of 3D simulations at 320 K SST to test the robustness of our findings. In 3D simulations, the domain size is 8,192 km by 8,192 km, with a horizontal resolution of 4 km. Other model setups are the same as 2D simulations. Due to the extensive computational resources consumed, we only test the role of radiative feedbacks at 320 K using 3D control and mechanism-denial experiments.

3.2 Metrics to Monitor CSA Development

We use column relative humidity (CRH) and its variance to visualize the development of CSA. CRH is the ratio of the precipitable water to the saturation water vapor path in the atmospheric column (Bretherton et al., 2005; Shamekh et al., 2020; Wing et al., 2020). It measures to what extent the air column is saturated. CRH always varies from 0 to 1 and allows us to compare the development of CSA over different climates.

4. Results

In this section, we will present the results of 2D and 3D simulations and the LMSE variance analysis, which demonstrate how radiative feedbacks play a decreasing role in the development of CSA with warming.

210

211 4.1 The 2D control experiments

212 CSA occurs in all examined climates in 2D control experiments. Figures 1a-e show the Hovmöller
213 diagrams of CRH in all climates. Initially, the distribution of CRH is homogenous over the domain,
214 and the CRH variance is close to zero (solid lines; Figure 1k). Within 20 days, the CRH variance
215 increases substantially over time, and the domain is divided into convection-active regions (blue;
216 moist) and convection-suppressed regions (white; dry). There is slight shifting and oscillation of
217 dry and moist regions in all climates, which may result from the propagation of gravity waves and
218 the oscillation of background winds. At the end of each simulation, the CRH variance oscillates
219 around a reference value.

220

221 The horizontal scale of CSA is defined as the average distance between adjacent moist centers,
222 which varies from 1,000 to 16,000 km in the 2D simulations and varies non-monotonically with
223 SST (Figures a-e). This non-monotonical behavior is similar to the results of Yang (2018), who
224 found that the horizontal scale depends on the boundary layer height, which decreases with rising
225 SSTs, and the density differences between moist and dry centers in the boundary layer, which
226 increase with SSTs.

227

228 4.2 The budget analysis of the LMSE variance

229 Then we analyze the budget of the LMSE variance in the 2D control experiments (Equation (4))
230 to quantify the contribution of different processes to the development and maintenance of CSA
231 (Figure 2). In the development stage, LMSE variance increases with time, and thus the growth rate
232 is positive. In the maintenance stage, the system reaches an equilibrium, and thus the growth rate

is close to zero. Apart from the growth rate, the budget analyses in the two stages are very similar: contribution from individual processes has similar values in the two stages at a given climate state.

Figure 2 shows that the contribution from adiabatic processes increases monotonically with warming in both the development and maintenance stages. The sign of adiabatic LMSE variance production switches from negative to positive at around 300 K. It suggests that, in colder climates, adiabatic processes transport LMSE from moist to dry regions (downgradient) and consume LMSE variance, while in warmer climates, it transfers LMSE from dry to moist regions (upgradient), increasing LMSE variance. Both changes in horizontal and vertical advection contribute to the sign switch. Here the steepening of the domain-mean MSE profile with warming in the boundary layer can lead to the increase of the LMSE variance production due to vertical advection (Arnold et al., 2013). This may be viewed as the decrease of gross moist stability in a warmer climate. However, as a common practice (Bretherton et al., 2005; Wing and Emanuel, 2014), we calculated the advection terms as a residual to close the budget, preventing us to perform a further decomposition and to test this hypothesis. An online diagnosis in the future will help further verify this hypothesis.

Additionally, Figure 2 shows that the total diabatic LMSE variance production, particularly radiative production, decreases with SSTs in both the development and maintenance stages. Radiative production is mostly positive in all climates, promoting the development of CSA. In colder climates, radiative production dominates the LMSE variance production, while in warmer climates, radiative production only has a minor contribution.

Figure 3 shows that the amplitude of MSE anomalies increases by an order of magnitude with 40-K SST warming, due to an increase in saturation vapor pressure. Meanwhile, the overall magnitude of radiative heating anomalies remains almost unchanged. To the leading order, that explains why the normalized radiative LMSE variance production (Equation (4)) decreases with warming. Previous research showed that the decrease in the role of radiative feedbacks mainly came from the decrease in the high-cloud fraction (Pope et al., 2021; Pope et al., 2023), which is also present in our simulations (black lines in Figure 3). Additionally, changes in the vertical structure of radiative anomalies further reduce the role of radiative feedbacks. For example, in colder climates, radiative heating anomalies are significant in the lower troposphere of the dry region, which is associated with low-cloud top radiative cooling. However, as the climate warms, the boundary layer becomes shallower (Yang, 2018a), and the associated low-cloud top radiative cooling also shifts to a lower altitude (black curves in Figure 3). Meanwhile, positive radiative heating anomaly emerges above the low clouds in the dry region at 310 and 320 K. Such rich vertical structures of radiative heating anomalies lead to a negative correlation locally between radiative anomalies and MSE anomalies right above low clouds of the dry region, further reducing radiative production in warmer climates.

Furthermore, Figure 2 shows that SGS processes play a vital role in damping LMSE variance in most climates, whose negative contribution comes from both surface fluxes and other SGS processes in the boundary layer (Supporting Information S1; Figures S1-S2).

Based on these findings, we hypothesize: in the absence of radiative feedbacks, CSA would disappear in colder climates but would still emerge in warmer climates. We will test our hypothesis using mechanism-denial experiments in the following section.

4.3 The 2D mechanism-denial experiments

The mechanism-denial experiments validate our hypothesis based on the LMSE variance analysis. Figures 1f and 1g show that CSA disappears at 280 and 290 K when we horizontally homogenize radiative heating rates. Gravity waves travel over the domain and form large-scale interference patterns at 280 and 290 K. Their moisture distributions seem distinct from that of the conventional moisture aggregation in the control simulations, resulting in lower CRH variance (Figure 1k). At 300 K, the CRH field exhibits a combination of gravity waves and weak, short-lived aggregation (Figures 1h), also yielding a lower CRH variance compared to the control experiment. In warmer climates, CSA is more visible without radiative feedbacks (Figures 1i-j and A1). At 310 K, stationary dry and moist signals are visibly present, e.g., from day 50 to day 100 at about x = 5,000 km, although the CRH variance in the mechanism-denial experiment remains smaller than the control experiment. At 315 K (Figure S3) and 320 K, stationary aggregation signals reach a similar or even higher intensity than in the control experiment. These results support that radiative feedbacks favor the development of CSA in colder climates, but its effect decreases and is not essential in warmer climates.

Interestingly, the horizontal scale of CSA at 315 and 320 K increases significantly after we turn off radiative feedbacks (Figures 1e and 1j). The result may suggest that radiative feedbacks still

299 influence CSA features in a warmer climate, even though it is no longer essential to the
300 development and maintenance of CSA.
301
302 4.4 The 3D experiments
303 We further conduct 3D simulations at 320 K to test the robustness of our findings in 2D. The size
304 of the largest convective cluster reaches 6,000 km in the 2D experiment at 320 K (Figure 1j).
305 Therefore, we use a domain of 8,192 km by 8,192 km to accommodate CSA. Due to the extensive
306 computational resources consumed, we only test the role of radiative feedbacks in 3D at 320 K.
307
308 Our results demonstrate that CSA still occurs without radiative feedbacks in 3D simulations at the
309 SST of 320 K. The CRH variance in both control and mechanism-denial experiments increases
310 monotonically with time. The mechanism-denial experiment reaches a higher degree of
311 aggregation by the end of the simulation, although it shows a slower growth in CRH variance from
312 day 8 to day 35 (Figures 4a). Additionally, the 3D domain is divided into dry and moist regions in
313 the two simulations. The horizontal scale of CSA is around 2,000 km in the control experiment
314 (Figure 4b) and around 6,000 km in the mechanism-denial experiment (Figure 4c). Such slower
315 growth of CRH variance in the development stage and larger horizontal scale in the mechanism-
316 denial experiment in 3D agrees with 2D results. Therefore, 3D simulations further support 2D
317 findings that radiative feedbacks are not essential to development in a warmer climate.
318
319 5. Conclusion and Discussion
320 This paper tests the hypothesis that radiative feedbacks are essential to the development of CSA.
321 To achieve this goal, we perform 2D and 3D CRM simulations and analyze the LMSE variance

budget (Yao, Yang and Tan, 2022) to quantify the contributions of different processes to CSA in a wide range of climates. Unlike conventional MSE variance analysis (Wing and Emanuel, 2014), the LMSE analysis respects the characteristic vertical structures of CSA, including its MSE anomaly and associated sources. which has been proven crucial to the development of CSA (e.g., Muller and Held, 2012). The LMSE analysis shows that the role of radiative feedbacks decreases with warming, and this is further supported by the mechanism-denial experiments. For example, CSA does not occur in colder climates at SSTs of 280 and 290 K without radiative feedbacks, but convection still aggregates in warmer climates with horizontally homogenized radiation, suggesting that radiative feedbacks are no longer essential to the development of CSA in warmer climates. This result broadly agrees with the view that CSA can arise from the interaction between atmospheric convection and its large-scale environment (Craig and Mack, 2013; Tompkins and Semie, 2017; Yang, 2018b; Haerter, 2019; Yang, 2019, Windmiller and Craig, 2019; Yang, 2021; Muller et al., 2022).

Most of the study focuses on analyzing 2D CRM simulations because it is computationally expensive to perform large-domain 3D CRM simulations. However, to test the robustness of our results, we have performed a pair of 3D simulations at 320 K SST, showing that CSA can self-emerge without radiative feedbacks. The results agree well with our 2D CRM results. This finding may justify the use of 2D CRMs to study convective aggregation, which are more computationally efficient.

Our study helps to establish a further connection between the physics of CSA to that of TCs and the MJO. Research showed that TCs and the MJO could spontaneously develop under uniform

boundary conditions and suggested that TCs and the MJO are thus special forms of CSA in Earth's atmosphere (Bretherton et al., 2005; Nolan et al., 2007; Boos et al., 2016; Arnold and Randall, 2015). Interestingly, both TCs and the MJO can emerge without radiative feedbacks, as demonstrated by studies using CRMs (Reyes and Yang, 2020, Wing et al., 2016, and Muller and Romps, 2018), as well as super-parameterized GCMs (Arnold and Randall, 2015, and Yang and Hannah, 2022). In this study, we show that CSA can emerge under similar conditions, suggesting that the underlying physics of the three distinct phenomena may share a common foundation.

Acknowledgments. This work was supported by the Packard Fellowship for Science and Engineering (to D.Y.). The authors thank S. Seidel and Z.H. Tan for the input to improve the manuscript.

Data Availability Statement

The model setup scripts and analysis code are available at https://github.com/linyao1999/CSA_2023_codes.git.

360 **REFERENCES**

361 Andersen, J. A., and Z. Kuang, 2012: Moist static energy budget of MJO-like disturbances in the
362 atmosphere of a zonally symmetric aquaplanet. J. Climate, 25, 2782–2804,
363 https://doi.org/10.1175/JCLI-D-11-00168.1.

364 Arnold, N. P., and D. A. Randall, 2015: Global-scale convective aggregation: Implications for
365 the Madden-Julian oscillation. J. Adv. Model. Earth Syst., 7, 1499–1518,
366 https://doi.org/10.1002/2015MS000498.

367 ——, Kuang, Z., & Tziperman, E. (2013). Enhanced MJO-like variability at high SST. Journal
368 of Climate, 26(3), 988–1001. https://doi.org/10.1175/JCLI-D-12-00272.1.

369 Boos, W. R., A. Fedorov, and L. Muir, 2016: Convective self-aggregation and tropical
370 cyclogenesis under the hypohydrostatic rescaling. J. Atmos. Sci., 73, 525–544,
371 https://doi.org/10.1175/JAS-D-15-0049.1.

372 Bretherton, C. S., P. N. Blossey, and M. Khairoutdinov, 2005: An energy-balance analysis of
373 deep convective self-aggregation above uniform SST. J. Atmos. Sci., 62, 4273–4292,
374 https://doi.org/10.1175/JAS3614.1.

375 Collins, W. D., and Coauthors, 2006: The formulation and atmospheric simulation of the
376 Community Atmosphere Model version 3 (CAM3). J. Clim., 19, 2144–2161,
377 https://doi.org/10.1175/JCLI3760.1.

378 Coppin, D., and S. Bony, 2015: Physical mechanisms controlling the initiation of convective
379 self-aggregation in a general circulation model. J. Adv. Model. Earth Syst., 7, 2060–2078,
380 https://doi.org/10.1002/2015MS000571.

Craig, G. C., & Mack, J. M. (2013). A coarsening model for self-organization of tropical convection. Journal of Geophysical Research: Atmospheres, 118, 8761–8769. https://doi.org/10.1002/jgrd.50674.

Emanuel, K., A. A. Wing, and E. M. Vincent, 2014: Radiativeconvective instability. J. Adv. Model. Earth Syst., 6, 75–90, https://doi.org/10.1002/2013MS000270.

Haerter JO. 2019: Convective self-aggregation as a cold pool-driven critical phenomenon. Geophys. Res. Lett., 46(7), 4017–28, https://doi.org/10.1029/2018GL081817.

Holloway, C. E., and S. J. Woolnough, 2016: The sensitivity of convective aggregation to diabatic processes in idealized radiative-convective equilibrium simulations. J. Adv. Model. Earth Syst., 8, 166–195, https://doi.org/10.1002/2015MS000511.

Khairoutdinov, M. F., and D. A. Randall, 2003: Cloud resolving modeling of the ARM summer 1997 IOP: Model formulation, results, uncertainties, and sensitivities. J. Atmos. Sci., 60, 607–625, https://doi.org/10.1175/1520-0469(2003)060<0607:CRMOTA>2.0.CO;2

Kuang, Z., 2008: A moisture-stratiform instability for convectively coupled waves. J. Atmos. Sci., 65(3), 834–854, https://doi.org/10.1175/2007JAS2444.1.

Muller, C., and D. M. Romps, 2018: Acceleration of tropical cyclogenesis by self-aggregation feedbacks. Proc. Natl. Acad. Sci. USA, 115, 2930–2935, https://doi.org/10.1073/pnas.1719967115.

Muller, C., and I. M. Held, 2012: Detailed investigation of the self-aggregation of convection in cloud-resolving simulations. J. Atmos. Sci., 69, 2551–2565, https://doi.org/10.1175/JAS-D-11-0257.1.

Muller, C., D. Yang, G. Craig, T. Cronin, B. Fildier, J. O. Haerter, et al. 2022: Spontaneous aggregation of convective storms. Annual Review of Fluid Mechanics, 54(1), 133–157, https://doi.org/10.1146/annurev-fluid-022421-011319.

Nolan, D. S., E. D. Rappin, and K. A. Emanuel, 2007: Tropical cyclogenesis sensitivity to environmental parameters in radiative-convective equilibrium. Quart. J. Roy. Meteor. Soc., 133, 2085–2107, https://doi.org/10.1002/qj.170.

Pope, K. N., C. E. Holloway, T. R. Jones, and T. H. M. Stein, 2023: Radiation, clouds, and self-aggregation in RCEMIP simulations. Journal of Advances in Modeling Earth Systems, 15, e2022MS003317. https://doi. org/10.1029/2022MS003317.

Pope, K. N., C. E. Holloway, T. R. Jones, and T. H. M. Stein, 2021: Cloud-radiation interactions and their contributions to convective self-aggregation. Journal of Advances in Modeling Earth Systems, 13, e2021MS002535. https://doi. org/10.1029/2021MS002535.

Pritchard, M.S. and D. Yang, 2016: Response of the Superparameterized Madden–Julian Oscillation to Extreme Climate and Basic-State Variation Challenges a Moisture Mode View. Journal of Climate, 29, 4995–5008. https://doi: 10.1175/JCLI-D-15-0790.1.

Reyes, A. R. and D. Yang, 2020: Spontaneous cyclogenesis without radiative and surface-flux feedbacks. Journal of Climate, 78(12), 4169– 4184. https://doi.org/10.1175/JAS-D-21-0098.1.

Shamekh, S., Muller, C., Duvel, J.-P., & d'Andrea, F., 2020: Self-aggregation of convective clouds with interactive sea surface temperature. Journal of Advances in Modeling Earth Systems, 12(11), e2020MS002164. https://doi.org/10.1029/2020ms002164.

Tompkins, A. M.,2001: Organization of tropical convection in low vertical wind shears: The role of water vapor. Journal of the Atmospheric Sciences, 58(6), 529–545, https://doi.org/10.1175/1520-0469(2001)058h0529:OOTCILi2.0.CO;2.

——, and Addisu G. Semie, 2017: Organization of tropical convection in low vertical wind shears: Role of updraft entrainment. J. Adv. Mod. Earth Sys., 9, 1046–1068, http://dx.doi.org/10.1002/2016MS000802.

Wheeler, M., and G.N. Kiladis, 1999: Convectively coupled equatorial waves. Analysis of clouds and temperature in the wavenumber–frequency domain. J. Atmos. Sci., 56, 374-399, 10.1175/1520-0469(1999)056,0374:CCEWAO.2.0.

Windmiller, J. M., & Craig, G. C. (2019). Universality in the spatial evolution of self-aggregation of tropical convection. Journal of the Atmospheric Sciences, 76(6), 1677–1696. https://doi.org/10.1175/JAS-D-18-0129.1.

Wing, A. A., and K. A. Emanuel, 2014: Physical mechanisms controlling self-aggregation of convection in idealized numerical modeling simulations. J. Adv. Model. Earth Syst., 6, 59–74, https://doi.org/10.1002/2013MS000269.

——, and T. W. Cronin, 2016: Self-aggregation of convection in long channel geometry. Quart. J. Roy. Meteor. Soc., 142, 1–15, https://doi.org/10.1002/qj.2628.

——, C. L. Stauffer, T. Becker, K. A. Reed, M.-S. Ahn, N. P. Arnold, et al. (2020). Clouds and convective self-aggregation in a multimodel ensemble of radiative-convective equilibrium simulations. Journal of Advances in Modeling Earth Systems, 12(9), e2020MS002138. https://doi.org/10.1029/2020ms002138.

444 ——, S. J. Camargo, and A. H. Sobel, 2016: Role of radiative–convective feedbacks in
445 spontaneous tropical cyclogenesis in idealized numerical simulations. J. Atmos. Sci., 73,
446 2633–2642, https://doi.org/10.1175/JAS-D-15-0380.1.
447 Yang, D., 2018a: Boundary layer height and buoyancy determine the horizontal scale of
448 convective self-aggregation. J. Atmos. Sci., 75, 469–478, https://doi.org/10.1175/JAS-D-17-
449 0150.1.
450 ——, 2018b: Boundary layer diabatic processes, the virtual effect, and convective self-
451 aggregation. J. Adv. Model. Earth Syst., 10, 2163–2176,
452 https://doi.org/10.1029/2017MS001261.
453 ——, 2019: Convective heating leads to self-aggregation by generating available potential
454 energy. Geophysical Research Letters, 46(17–18), 10687–10696,
455 https://doi.org/10.1029/2019GL083805
456 ——, 2021: A shallow-water model for convective self-aggregation. J. Atmos. Sci., 78, 571–582,
457 https://doi.org/10.1175/JAS-D-20-0031.1.
458 ——, and W. Hannah, 2022: Vertically resolved analysis of the Madden-Julian Oscillation
459 highlights the role of convective transport of moist static energy. Paper presented at 23rd
460 Conf. on Atmos. and Oceanic Fluid Dynamics. 2022, Breckenridge, CO, Amer. Meteor.
461 Soc., 8.1, https://ams.confex.com/ams/23FLUID/meetingapp.cgi/Paper/403780.
462 Yao, L., D. Yang, and Z.-M. Tan, 2022: A vertically resolved MSE framework highlights the
463 role of the boundary layer in convective self-aggregation. J. Atmos. Sci., 79, 1615–1631,
464 https://doi.org/10.1175/JAS-D-20-0254.1.

Zhang, B., Soden, B. J., Vecchi, G. A., and Yang, W., 2021: The role of radiative interactions in tropical cyclone development under realistic boundary conditions. Journal of Climate, 34(6), 2079–2091. https://doi.org/10.1175/jcli-d-20-0574.1.

——, Soden, B. J., and Vecchi, G. A., 2022: A Vertically Resolved Analysis of Radiative Feedbacks on Moist Static Energy Variance in Tropical Cyclones. Journal of Climate, 36(4), 1125-1141. https://doi.org/10.1175/JCLI-D-22-0199.1.

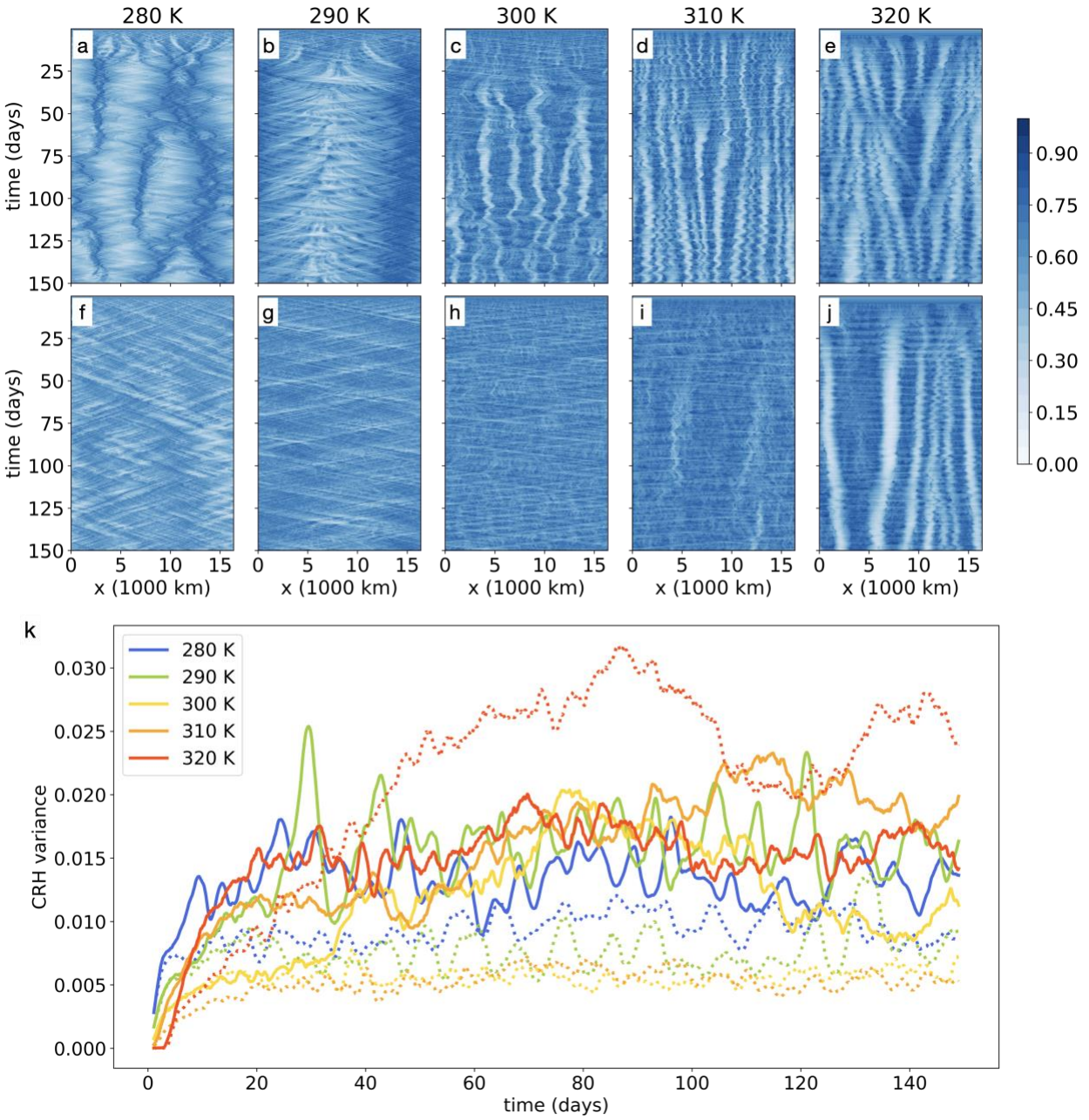

Figure 1. (a)-(j) are Hovmöller diagrams of column relative humidity (CRH) in the 2D control (the first row) and mechanism-denial experiments (the second row) over different climates (left to right: 280-320 K). (k) is the evolution of CRH variances in the 2D control (solid) and mechanism-denial experiments (dotted) over different climates.

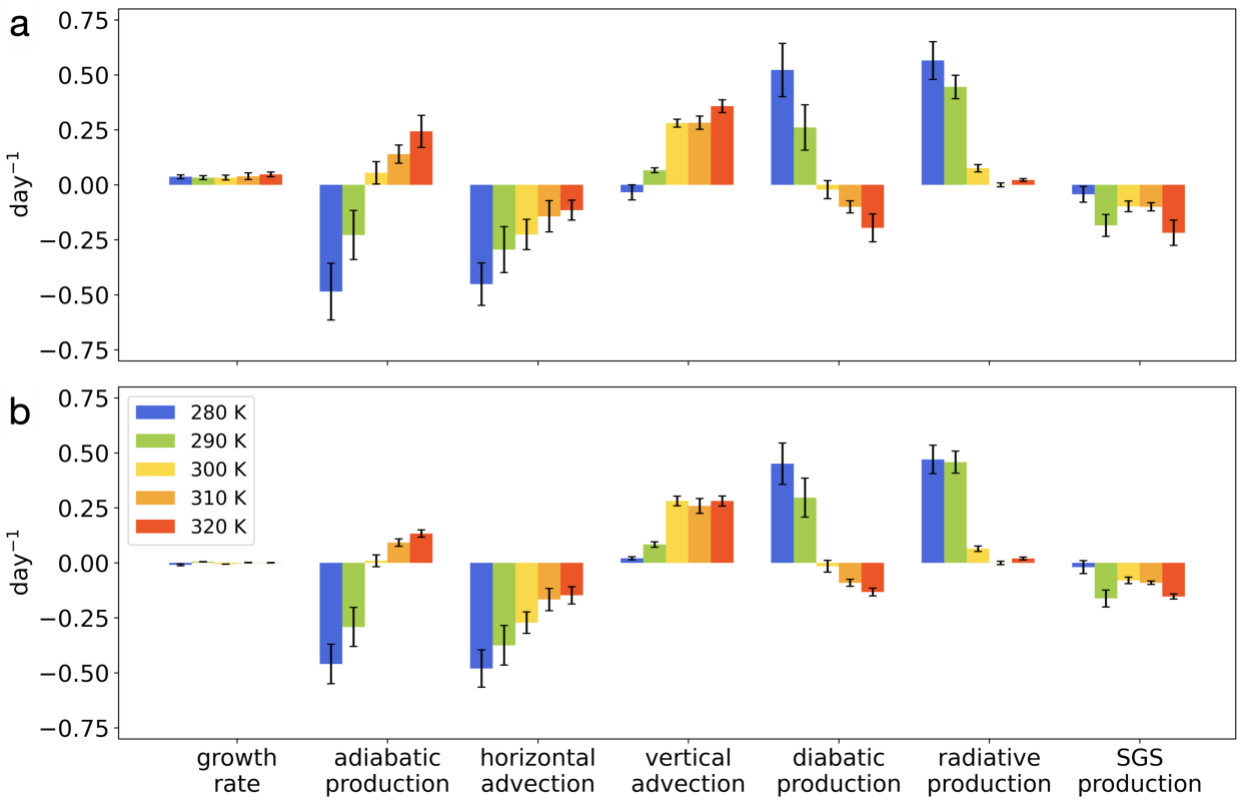

476

477 **Figure 2.** The LMSE variance analysis for 2D control experiments (Equation (4)). The upper panel
478 shows the budget averaged in the development stage, and the lower panel shows that averaged in
479 the maintenance stage. The error bars show uncertainty by using different window lengths of
480 temporal and special running averages (varying from 1 day to 10 days, from 40 km to 120 km) to
481 get large-scale perturbations and using different window lengths (varying from 5, 10, 15, 20, to 25
482 days) to average the LMSE budget in the development and maintenance stages. The 'adiabatic
483 production' represents the total contribution from horizontal and vertical advection processes. The
484 'diabatic production' represents the total contribution from radiation and SGS processes.

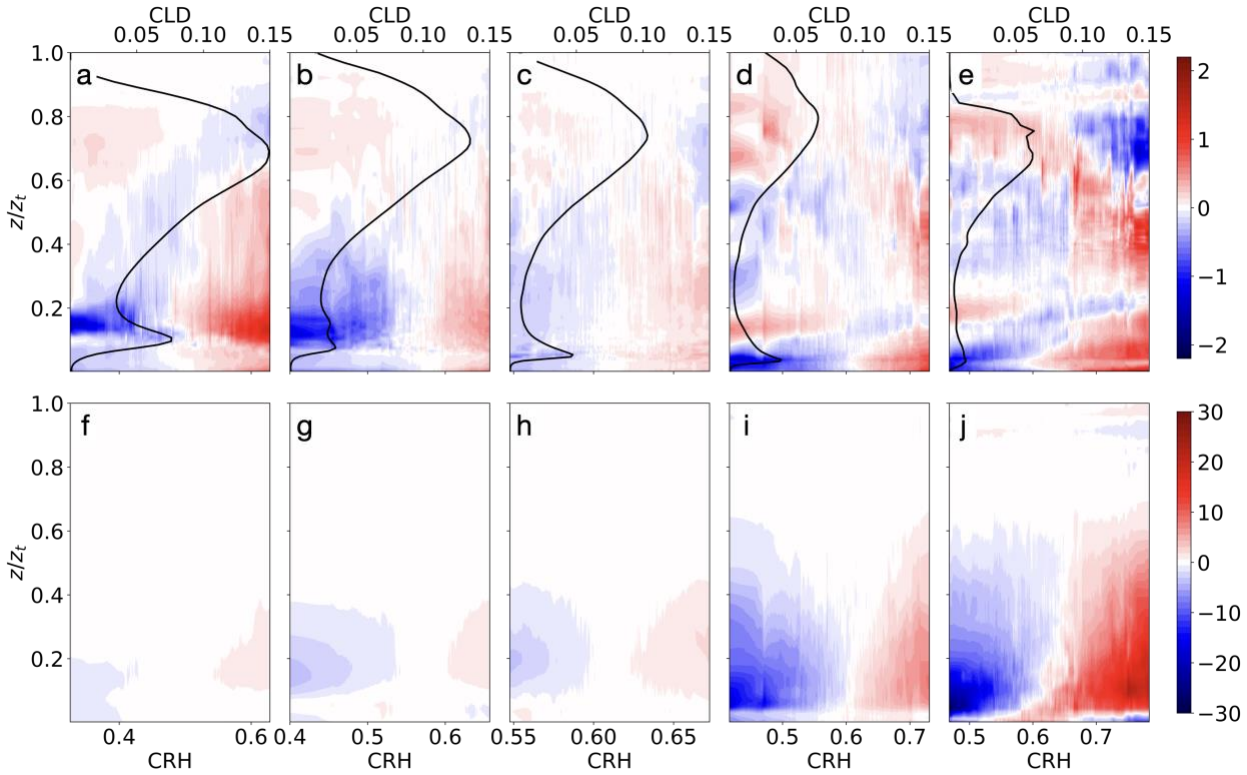

485

486 **Figure 3.** The distributions of (a-e) radiative heating anomalies (K day^{-1}) and (f-j) MSE

487 anomalies (K) over different climates (left to right: 280-320 K) in the development stage. The

488 black lines in (a)-(e) show domain-averaged cloud fractions in respective climates.

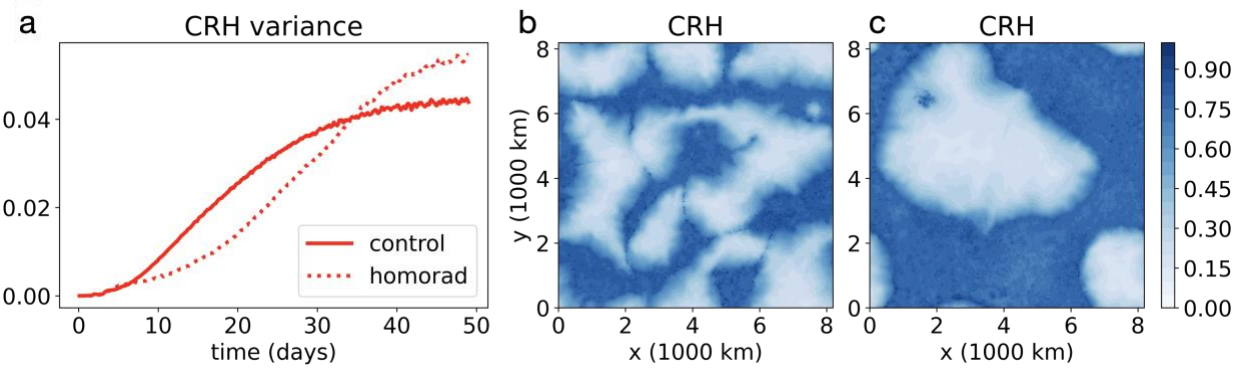

489

490 **Figure 4.** (a) The evolution of the spatial variances of CRH in 3D experiments at 320 K. 'homorad'
491 means we homogenize radiative profiles in the mechanism-denial experiment. The snapshots of
492 CRH at day 49 in the 3D (b) control and (c) mechanism-denial experiments.